Journal of Materials Chemistry A

PAPER

View Article Online
View Journal | View Issue

Check for updates

Cite this: J. Mater. Chem. A, 2018, 6, 23659

A free standing Ru–TiC nanowire array/carbon textile cathode with enhanced stability for Li–O_2 batteries†

Chenjuan Liu,[a] Zhen Qiu,[b] Willian R. Brant,[a] Reza Younesi,[a] Yue Ma,[c] Kristina Edström,[a] Torbjörn Gustafsson[a] and Jiefang Zhu *[a]

Received 13th December 2017
Accepted 24th October 2018

DOI: 10.1039/c7ta10930j

rsc.li/materials-a

The instability of carbon cathode materials is one of the key problems that hinder the development of lithium–air/lithium–oxygen (Li–O_2) batteries. In this contribution, a type of TiC-based cathode is developed as a suitable alternative to carbon based cathodes, and its stability with respect to its surface properties is investigated. Here, a free-standing TiC nanowire array cathode was *in situ* grown on a carbon textile, covering its exposed surface. The TiC nanowire array, *via* deposition with Ru nanoparticles, showed enhanced oxygen reduction/evolution activity and cyclability, compared to the one without Ru modification. The battery performance of the Li–O_2 cells with Ru–TiC was investigated by using *in operando* synchrotron radiation powder X-ray diffraction (SR-PXD) during a full cycle. With the aid of surface analysis, the role of the cathode substrate and surface modification is demonstrated. The presented results are a further step toward a wise design of stable cathodes for Li–O_2 batteries.

Open Access Article. Published on 24 October 2018. Downloaded on 6/14/2026 1:53:30 PM.
This article is licensed under a Creative Commons Attribution 3.0 Unported Licence.

Introduction

Non-aqueous Li–air (Li–O_2) batteries have been considered as a promising candidate for energy storage due to their significantly higher theoretical energy density, compared to conventional Li-ion batteries.[1,2] The functioning of a Li–O_2 battery relies on the reversible deposition and decomposition of the discharge product, Li_2O_2, on the surface of the cathode during cycling. Although the working mechanism of Li–O_2 batteries appears straightforward, some challenges, such as low energy efficiency, high over-potential, and poor cyclability, hinder the commercialization of Li–O_2 batteries. Today, it is well accepted that these problems mostly originate from the nature of the discharge products. These partly reduced oxygen species are highly reactive, can attack the electrolyte and the cathode, and induce irreversible side reactions.[3] Up to now, some progress has been achieved in improving the electrochemical performance of Li–O_2 batteries during both discharge and charge.[4,5] However, fundamental questions remain, concerning the chemical and electrochemical stability of all functional components during cycling.[6–10]

In this study, with the aid of the SR-PXD technique, we focus on improving cathode stability. Among all cathode materials, carbon is mostly used in non-aqueous Li–O_2 batteries due to its abundance, light weight, high conductivity and tuneable porous structure.[11–13] However, many groups have identified the instability of the carbon materials that have been used in the Li–O_2 system.[14,15] Consequently, a few strategies have been tried, aimed at increasing the cathode substrate stability.[16–19] Owing to their outstanding anti-corrosion ability and good conductivity, carbides as a cathode material have recently aroused increasing interest.[18,20,21] TiC was reported as a promising cathode material when coupled with a DMSO electrolyte and a $LiFePO_4$ anode, showing >98% capacity retention after 100 cycles.[18] This excellent performance was attributed to the good electronic conductivity of TiC and the stability of a TiO_2-rich layer formed on the TiC surface. Later, Adams *et al.* showed that the oxygen evolution reaction (OER) upon charging was strongly dependent on the TiC cathode surface properties. The thickness of the TiO_2 layer on the TiC surface was a key parameter determining the function of the TiC cathode.[21] Kozmenkova *et al.* found that a clean TiC surface could be easily oxidized by Li_2O_2, and an oxidation treatment using molecular oxygen could improve TiC stability. However, they also claimed that such a complicated protective coating procedure is not practically useful for a real battery system.[22] In addition, there are some shortcomings in the commonly used cathode design. Conventional cathodes with a powder and binder mixture introduce instability problems due to binder decomposition.[9,23]

[a]Department of Chemistry – Ångström Laboratory, Uppsala University, Box 538, SE-751 21 Uppsala, Sweden. E-mail: jiefang.zhu@kemi.uu.se; Fax: +46 18 51 3548; Tel: +46 18 471 3722

[b]Department of Engineering Sciences, Solid State Physics, Uppsala University, Box 534, 75121 Uppsala, Sweden

[c]State Key Laboratory of Solidification Processing, Center for Nano Energy Materials, School of Materials Science and Engineering, Northwestern Polytechnical University, 710072 Xi'an, China

† Electronic supplementary information (ESI) available. See DOI: 10.1039/c7ta10930j

Open Access Article. Published on 24 October 2018. Downloaded on 6/14/2026 1:53:30 PM.
This article is licensed under a Creative Commons Attribution 3.0 Unported Licence.

To facilitate electron transfer to and from insulating Li_2O_2 during cycling, a rational design of electronic and ionic pathways in cathodes is essential. Compared to powder particles, one-dimensional (1D) nanostructures on the cathode surface can offer directional charge transportation along the 1D structure, diminishing boundary resistance.[24,25] 1D nanostructures, *e.g.* nanowires, can provide facile charge transfer, exhibit improved surface chemistry and catalytic properties, and enhance the kinetics of electrochemical reactions.[26] Besides, a metallic current collector is normally used in a Li–O_2 battery, which increases the weight of the battery, thus decreasing the total gravimetric capacity. It would be very meaningful to replace metallic current collectors with light conductive materials.

The formation and decomposition of Li_2O_2 have been studied by *ex situ* X-ray diffraction (XRD), Raman spectroscopy, transmission electron microscopy (TEM), nuclear magnetic resonance spectroscopy, FT-IR and X-ray absorption near edge structure spectroscopy.[12,13,16,27–29] However, artifacts from sample preparation are difficult to avoid and very limited information on the operation mechanism and reaction kinetics of Li_2O_2 formation and oxidation could be obtained. *In operando* techniques including spectroscopy, microscopy and diffraction with their feature of collecting data during electrochemical cycling without unpacking the cell, have provided valuable information on the reversibility of Li_2O_2.[30–35] However, it is still difficult to obtain the quantified efficiency of the cell by these techniques. Although differential electrochemical mass spectroscopy (DEMS) can provide quantification information in real-time, the targets are limited to gas species which are only evolved from the charge process.[36] To date, only a few studies have successfully performed *in situ* or *in operando* measurement by in-house XRD to investigate the evolution of Li_2O_2.[37] However, due to the limited X-ray intensity of in-house X-ray sources and the poor scattering ability of Li_2O_2, a long irradiation time is required and the kinetic information obtained during the process is lost. As summarized in Table S1,† with a higher X-ray intensity and better time resolution, *in operando* synchrotron radiation powder X-ray diffraction (SR-PXD), which was recently developed by us,[38] can provide an efficient, accurate and reliable evaluation of the efficiency of Li–O_2 electrochemical reactions during both discharge and charge.

Based on the aforementioned considerations, we aim to design and fabricate an electrochemically stable and efficient cathode for Li–O_2 batteries. One of our co-authors developed a biotemplating method for TiC nanowire synthesis.[50] Inspired by that work, here a TiC nanowire array (TiC NA) with a TiO_2 surface layer was *in situ* grown on a carbon textile (CT). By this method, a binder-free cathode was obtained. Since the performance of Li–O_2 batteries largely hinges on the surface chemistry of the cathode, the surface of TiC NAs/CT was modified by loading Ru nanoparticles. Ru- or RuO_2 based electrocatalysts have been reported as bifunctional catalysts with a much lower cost compared to Pt, Pd and Au,[19,39,40] and do not promote electrolyte decomposition.[41] Galvanostatic tests and X-ray photoelectron spectroscopy (XPS) analysis confirmed the crucial effect of these Ru NPs. Unlike previous reports on TiC cathodes, this study features unique aspects: (1) the usage of polymer binders is avoided by the direct growth of TiC on the CT; (2) the flexible CT functions as a conductive backbone with its surface coated by TiC NAs, which act as a physical barrier to prevent the exposure of the carbon cloth to the electrolyte; (3) the surface of the TiC nanowires is decorated with Ru NPs, which enhance the electrochemical performance of the Li–O_2 battery and improve the stability of TiC during battery operation; (4) SR-PXD and in-house XRD quantitatively track the phase evolution inside the Li–O_2 battery.

Results and discussion

Characterization of Ru–TiC nanoarrays

The morphology of the as-prepared TiC electrode was investigated by scanning electron microscopy (SEM) and transmission electron microscopy (TEM). The pristine CT is composed of carbon fibres with a diameter about 8 μm (the inset of Fig. 1a). Fig. 1a–d show that the TiC NAs were grown homogeneously and perpendicular to the surface of the CT skeleton without using any binder. Here the CT served as both the current collector and the structural support of the TiC NAs. As shown in Fig. 1a–c, the whole piece of the CT is covered with TiC NAs with a length of 30–50 μm and a width of 200–500 nm. The cross section (the inset of Fig. 1b) of one TiC NAs/CT shows the core–shell configuration, which can not only protect the CT from attack by partly reduced oxygen species, but also facilitate electron transfer throughout the cathode. The two strong peaks at 1348 and 1590 cm^{-1} (Fig. 1g) correspond to the D and G bands of carbon cloth, respectively. The Raman spectra shown in Fig. 1g and h reveal that the D- and G-band from the pristine CT almost vanished in the TiC NAs/CT sample. The Raman peak at 144 cm^{-1} can be attributed to a small amount of rutile TiO_2 (as shown in Fig. S1†), while the peaks at 257, 424, and 604 cm^{-1} (Fig. 1h) are assigned to the vibration signals of TiC.[42] This indicates the effective coverage of the CT surface by the TiC NAs. The XRD (Fig. 1i) pattern shows that the as-prepared electrode consists of TiC and CTs. The pattern peaks at 36.0°, 41.8°, 60.7°, 72.6°, and 76.5° are indexed as the (111), (200), (220), (311), and (222) reflections of the cubic TiC ($Fm\bar{3}m$, ICSD # 1546), respectively. The HRTEM image taken from an individual TiC nanowire (Fig. 1d) shows that the *d*-spacing value of the adjacent lattice fringes is 0.246 nm, corresponding to the (111) lattice plane of the cubic TiC. Prior to Ru loading (Fig. 1c and d), the nanowires have a smooth surface. After loading Ru nanoparticles, the TiC nanowires still maintain the same shape (Fig. 1e and f), but the surface roughens due to the deposition of Ru nanoparticles. Fig. 1f shows the HRTEM image of Ru–TiC NAs/CT with a Ru particle size of about 2–5 nm. The lattice spacing values in Fig. 1f are 0.247 nm and 0.214 nm, corresponding to the (111) lattice plane of cubic TiC and (002) lattice plane of hexagonal-structured Ru ($P6_3/mmc$, ICSD # 40354), respectively. The EDS mapping (Fig. S2†) also shows the distribution of C, Ti, O, Ru, and Ni at the top part of the TiC NAs. The Ni NPs located at the tip of the TiC NAs (the inset of Fig. 1c) acted as the catalyst for the growth of the TiC NAs.[43,44]

 This journal is © The Royal Society of Chemistry 2018

Open Access Article. Published on 24 October 2018. Downloaded on 6/14/2026 1:53:30 PM.
This article is licensed under a Creative Commons Attribution 3.0 Unported Licence.

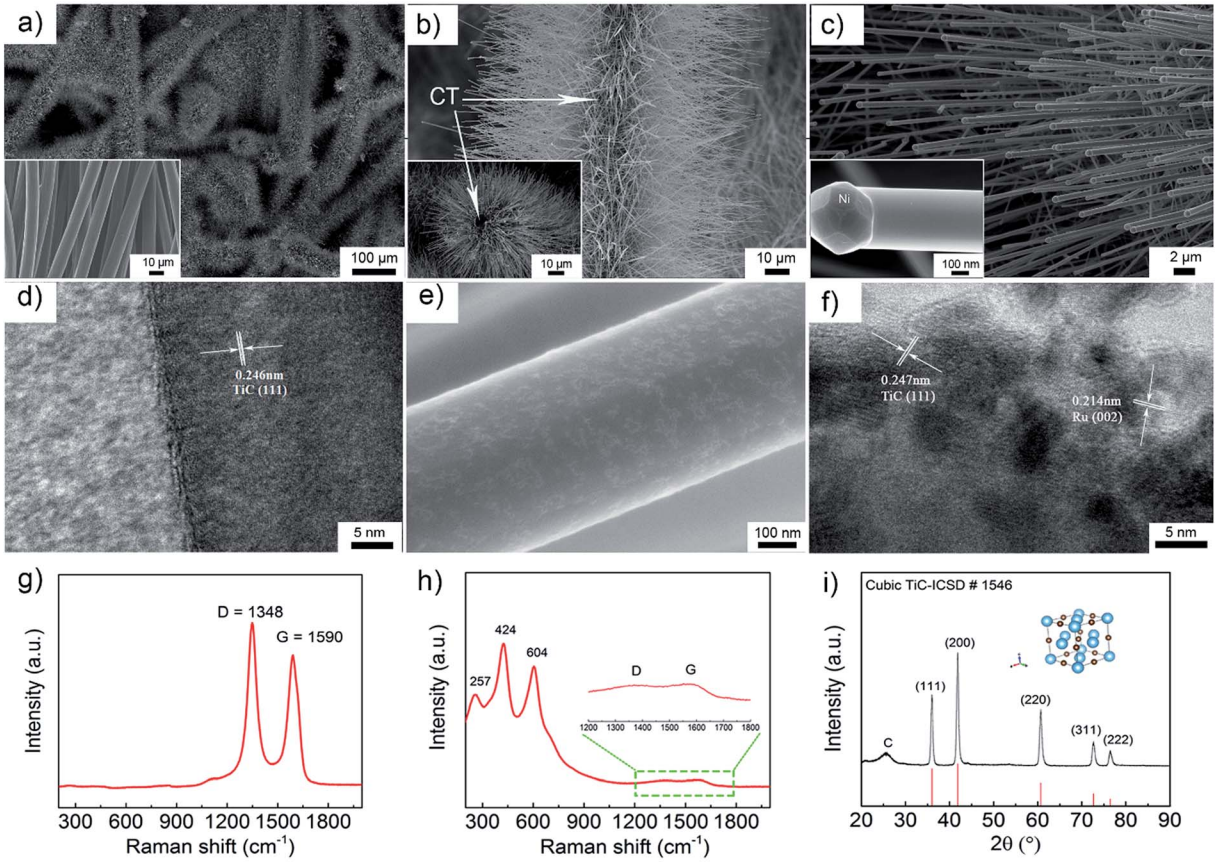

Fig. 1 (a–c) SEM images of TiC arrays on the carbon cloth textile with different magnifications. The inset of (a) shows the pristine CT, the inset of (b) shows a cross section of TiC NAs/CT and the inset of (c) shows the tip of a TiC nanowire. (d) High magnification TEM image of a TiC nanowire. High magnification (e) SEM and (f) TEM images of Ru/TiC. Raman spectra of (g) the pristine CT and (h) TiC NAs/CT. (i) XRD pattern ($\lambda = 1.5406$ Å) of the as-prepared TiC NAs/CT.

XPS was performed to investigate the elemental oxidation states and the surface composition of the as-prepared samples.

The C 1s core level XPS spectra of the pristine CT, TiC NAs/CT and Ru–TiC NAs/CT are compared in Fig. 2. For pristine CT, the carbon peak was deconvoluted into five peaks at 284.5 eV, 285.0 eV, 286.6 eV, 287.6 eV and 290.3 eV, assigned to C–C, C–H, C–O, O–C=O and $-CO_3$, respectively.[45] For the TiC NAs/CT composites, the C–Ti bond in the carbide phase and the C–C bond in the carbon matrix phase were clearly found at 281.6 eV and 284.5 eV, respectively. In addition, a contribution from TiO_xC_y at ~282.4 eV was observed in accordance with previous studies.[22] In Ru–TiC NAs/CT, the peaks at ~280.2 eV and ~284.4 eV can be attributed to the two spin orbit coupling peaks of Ru.

Efficiency of Li_2O_2 formation and decomposition

In operando SR-PXD ($\lambda = 0.994$ Å) was applied to track the evolution and quantify the amount of Li_2O_2 during the cycling of the Li–O_2 cell using a Ru–TiC NAs/CT cathode and 1 M $LiClO_4$ DMSO-based electrolyte. The cell was run for a complete discharge and charge cycle at a current density of 0.1 mA cm^{-2}. A series of diffraction patterns containing a Si peak and two Li_2O_2 peaks are shown in Fig. 3a. A known amount of Si was added as a reference to quantify the amount of Li_2O_2 during the cycling. When the Li–O_2 cell is discharged/charged with a constant current, a linear formation/decomposition of Li_2O_2 with time is expected in the absence of side reactions. According to our previous results, the amount of Li_2O_2 was fitted into two linear regions during discharge (Fig. 3b).[38] During the first discharge stage, the rate (the slope in Fig. 3b) of Li_2O_2 formation is $k_{f1} = 0.068$ mg h^{-1}, which is slightly lower than the theoretical value of $k_{theo} = 0.086$ mg h^{-1}. After about 10 hours of discharge, a lower formation rate was observed ($k_{f2} = 0.042$ mg h^{-1}). The decreasing formation rate is probably due to side reactions occurring during the later stage of discharge, such as the decomposition of the electrolyte. This two-stage model agrees with the two-step Li_2O_2 growth during discharge.[38] Due to an uncontrollable beam loss, we could not collect diffraction patterns from 14 h to 24 h, which covered the end of discharge and the beginning of charge. As charging proceeded, a linear decrease of the electrochemically formed Li_2O_2 can be observed during the later stage of the charge with $k_d = -0.073$ mg h^{-1}, which is close to the ideal decomposition rate of Li_2O_2, $k_{theo} = -0.086$ mg h^{-1}. This indicates an oxidation of bulk Li_2O_2 with fewer parasitic reactions. We also notice that the (101) diffraction peak of electrochemically formed Li_2O_2, at around 22° in Fig. 3a,

Open Access Article. Published on 24 October 2018. Downloaded on 6/14/2026 1:53:30 PM.
This article is licensed under a Creative Commons Attribution 3.0 Unported Licence.

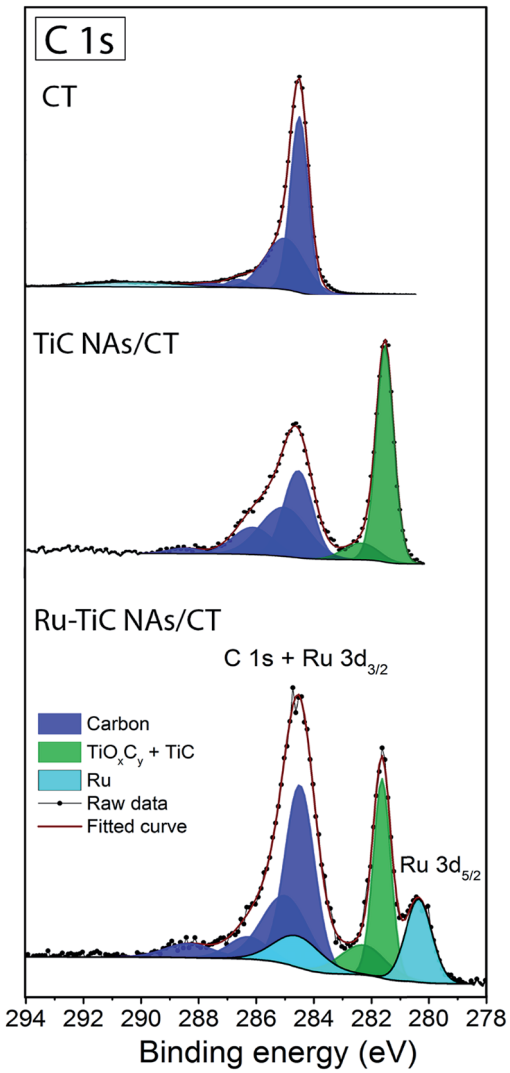

Fig. 2 C 1s and Ru 3d core-level XPS spectra of pristine CT, TiC NAs/CT and Ru–TiC NAs/CT fitted with multiple envelopes.

is broad and overlaps with the TiC (111) peak. This peak broadening does not affect the quantification, since the quantification refinement was determined by the integrated peak area.

To investigate the OER process while eliminating the influence of electrolyte decomposition on discharge, a cell with a Ru–TiC NAs/CT cathode loaded with crystalline commercial Li_2O_2 powder was studied from the beginning of the charging process. As the commercial Li_2O_2 has better crystallinity than the electrochemically formed one, sharper diffraction peaks were observed (Fig. 4a). This results in a better resolution between the Li_2O_2 (101) and the TiC (111) diffraction peaks. The fading of the diffraction peaks at 32.7° and 34.8° (X-ray wavelength $\lambda = 1.5406$ Å) in Fig. 4a, corresponding to the (100) and (101) peak of Li_2O_2 (ICSD # 25530 $P6_3/mmc$ space group), proves the electrochemical decomposition of Li_2O_2 during the charge process. Following the evolution of Li_2O_2 during charge (Fig. 4b), the oxidation of Li_2O_2 took place in two stages. The residual ratio of Li_2O_2 (calculation details are described in the ESI†) was static at the short initial step, and then declined linearly during the next stage. At the beginning of charging, the detected amount of Li_2O_2 was almost constant, probably due to the preferential decomposition of the surface impurities on Li_2O_2. The major stage shows a decomposition rate of -1.28 h^{-1}, and the theoretical value (-1.38 h^{-1}) is also given as a reference in Fig. 4b. This indicates that Ru–TiC NAs/CT is an efficient cathode, providing an oxidation efficiency around 93%. As demonstrated in Fig. 4b, the charge potential of the commercial Li_2O_2-loaded cell was higher than that with electrochemically formed Li_2O_2 shown in Fig. 3b, probably due to the larger particle size of commercial Li_2O_2 and its poorer contact with the electrode. Different from a carbon based electrode, we did not observe a sharp voltage rise and drop at the initial stage of charge here, which is due to the reaction between carbon and Li_2O_2 at their interface.[32] This further confirms the good protection of the carbon surface by the TiC NAs in the prepared samples.

Morphology evolution

Since Li_2O_2 is very sensitive to the electron beam of the TEM, which could lead to Li_2O_2 degradation,[46,47] SEM was employed to elucidate the morphological evolution of the discharge product after different stages of cycling. As shown in Fig. 5a and b, after the first discharge process, small particles were uniformly distributed on the Ru–TiC nanowire surface with an average size around 200 nm. These particles have been suggested to be Li_2O_2.[48,49] After the first charge process, the particles disappeared and the smooth Ru–TiC surface reappeared (Fig. 5c and d). During the second discharge process, as shown in Fig. 5e and f, Li_2O_2 appeared again. Overall, the SEM images confirmed that Li_2O_2 was reversibly formed and decomposed on the surface of Ru–TiC, at least for the first few cycles.

Battery performance

To highlight the merits of the as-prepared electrode, bare CT and TiC NAs/CT were used as the cathodes for comparison. Fig. 6a displays the complete discharge curves (with a cut off potential of 2.3 V) of the cells with bare CT, as-prepared TiC NAs/CT and Ru–TiC NAs/CT cathodes at a current density of 0.1 mA cm^{-2}. The Li–O_2 cell with pristine CT exhibits a capacity of about 0.6 mA h cm^{-2}, while the cells with TiC NAs/CT and Ru–TiC NAs/CT show a capacity of about 1.2 mA h cm^{-2} and 1.6 mA h cm^{-2}, respectively. According to the mass of TiC (determined from the thermal gravimetric analysis (TGA) in Fig. S3† and the inductively coupled plasma (ICP) analysis in Table S3†), the TiC NAs/CT and Ru–TiC NAs/CT cathodes showed a capacity of about 352 mA h g_{TiC}^{-1} and 468 mA h g_{TiC}^{-1}, respectively (corresponding to 155 mA h g^{-1} and 206 mA h g^{-1} based on the total weight of the cathode, respectively; ESI, Fig. S4†). The current density used here was about 29.3 mA g_{TiC}^{-1} (corresponding to 12.9 mA h g^{-1} based on the total weight of the cathode). The discharge voltage of Ru–TiC NAs/CT is slightly higher than those of pristine CT and TiC NAs/CT (Fig. 6b). This result was further supported by the electrochemical impedance spectroscopy (EIS) results in Fig. S5.† As shown in Fig. 6b, compared with using pristine CT,

 This journal is © The Royal Society of Chemistry 2018

Open Access Article. Published on 24 October 2018. Downloaded on 6/14/2026 1:53:30 PM.
This article is licensed under a Creative Commons Attribution 3.0 Unported Licence.

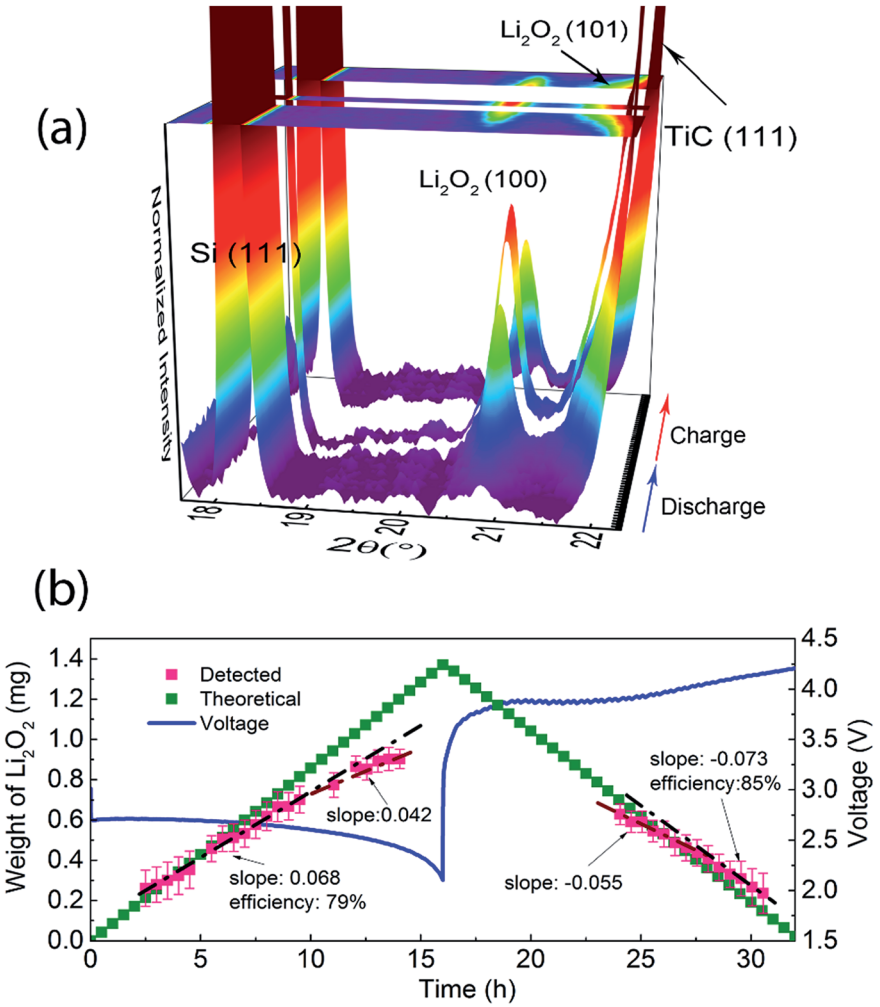

Fig. 3 (a) *In operando* SR-PXD pattern ($\lambda = 0.994$ Å) of a Ru–TiC NAs/CT based Li–O_2 battery, collected every 30 min during the first cycle at a constant current of 0.1 mA cm^{-2}, (b) galvanostatic discharge–charge voltage of the Li–O_2 cell and the Li_2O_2 mass evolution during the first cycle. The gap in the 3D plot and in the Li_2O_2 mass evolution corresponds to an unexpected beam loss.

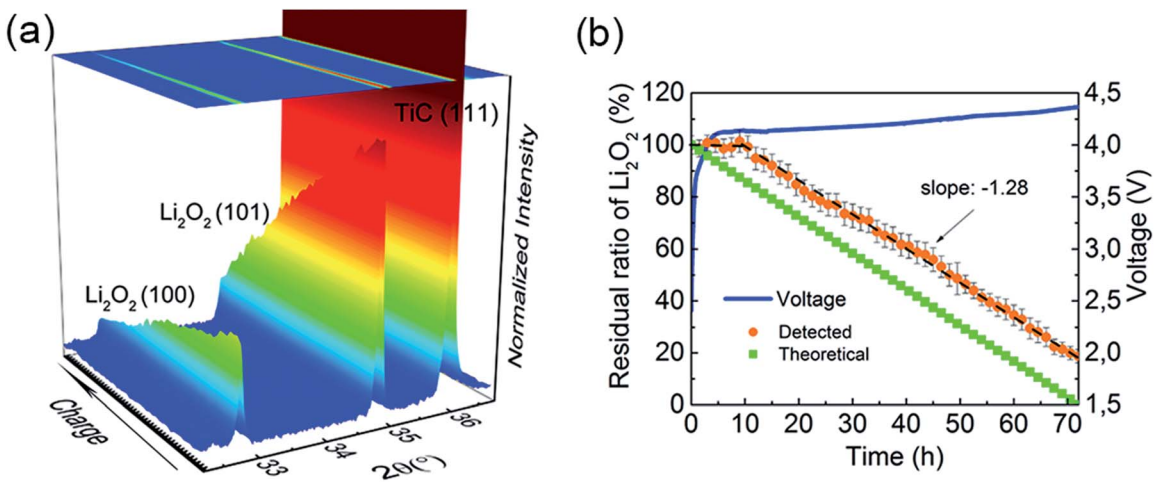

Fig. 4 Galvanostatic charging of commercial Li_2O_2. (a) 3D plots of the diffraction patterns ($\lambda = 1.5406$ Å) presented as a function of time during charge with a constant current of 0.2 mA cm^{-2}. (b) The charging profile, integrated curve and linear fitting of Li_2O_2 decomposition during the *in operando* XRD measurement.

Open Access Article. Published on 24 October 2018. Downloaded on 6/14/2026 1:53:30 PM.
This article is licensed under a Creative Commons Attribution 3.0 Unported Licence.

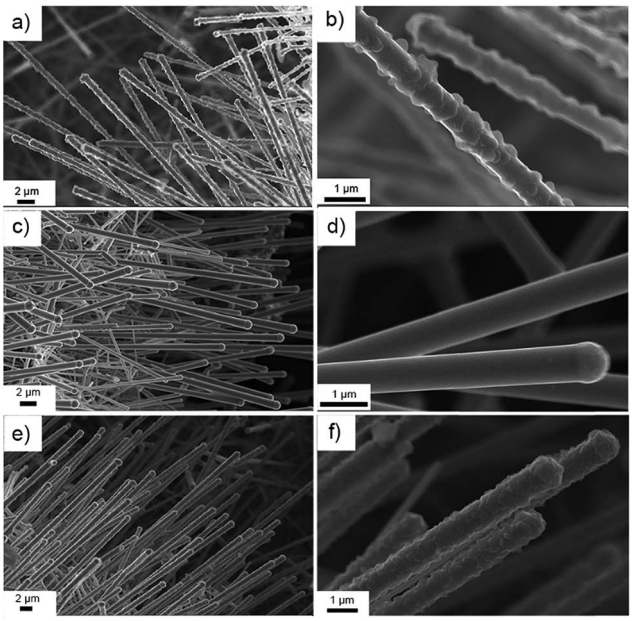

Fig. 5 SEM images with different magnifications of the Ru/TiC cathode after the (a and b) 1st discharge, (c and d) 1st charge, and (e and f) 2nd discharge at 0.05 mA cm^{-2} current density with a limited capacity of 0.2 mA h cm^{-2}.

the first discharge–charge overpotential can be significantly decreased by using TiC NAs/CT, and can be further reduced by using Ru–TiC NAs/CT. Based on the first discharge–charge curves in Fig. 6b, the overpotentials of the cells can be estimated to be ~1.65 V, ~1.12 V and ~0.91 V for the CT, TiC NAs/CT and Ru–TiC NAs/CT cathodes, respectively. The reduced overpotential of Ru–TiC NAs/CT can be ascribed to the intrinsic contact between the TiC NAs and the CT as well as the catalytic activity of Ru nanoparticle-modified TiC. In addition, the cyclic voltammetry (CV) measurements (Fig. S6†) also reveal that with Ru modification, the Ru–TiC NAs/CT cathode exhibits a higher catalytic activity, compared to the TiC NAs/CT cathode.

Considering the rate performance of the Ru–TiC NAs/CT cells as shown in Fig. S7,† a current density of 0.05 mA cm^2 was chosen to cycle all the batteries. The selected voltage profiles of the pristine CT, TiC NAs/CT and Ru–TiC NAs/CT cathodes with a limited capacity of 0.2 mA h cm^{-2} are presented in Fig. S8.† An increase in the discharge and charge potentials in the 260th cycle is observed with the Ru–TiC NAs/CT cathode, compared to the 10th cycle, which could be attributed to the electrolyte decomposition and the accumulation of side products during cycling. The capacity limiting cycling method applied here does not present the whole image of the cyclability of the Li–O_2 cell. A large number of cycles do not guarantee good reversibility, since they could still originate from side reactions. However, comparing the cycling performance for different cathode materials at the same cycling conditions can, to some extent, reflect the activity and the stability of the cathode materials toward the Li_2O_2 formation and decomposition process. As summarized in Fig. 6c, with the same current density and capacity limitation, the cell with Ru–TiC NAs/CT can operate for around 270 cycles, which is much longer than for the cells with TiC NAs/CT (around 125 cycles) and pristine CT electrodes (about 15 cycles). The charge potentials of all the cells decreased during the first few cycles and then increased continuously upon cycling. As shown in Fig. 6c, the average charge potential of the cell with Ru–TiC NAs/CT is lower than those of the cells with TiC NAs/CT and pristine CT. To calculate the round-trip efficiencies, the average discharge potential was divided by the average charge potential, and the results are shown in Fig. 6c. The round-trip efficiency of the cell with Ru–TiC NAs/CT is consistently higher than those of the cells with TiC NAs/CT and pristine CT. In addition, the instability of the cell with the CT electrode was also revealed by *ex situ* XRD results. As shown in Fig. S9,† LiOH was formed during discharge, which indicates the instability of the DMSO electrolyte in contact with the carbon cathode.

Stability information from the XPS study

The stability of the TiC cathode in Li–O_2 batteries was reported to be related to the surface chemistry, where a layer of TiO_2 was formed during cycling.[18,22] However, the thickness of the

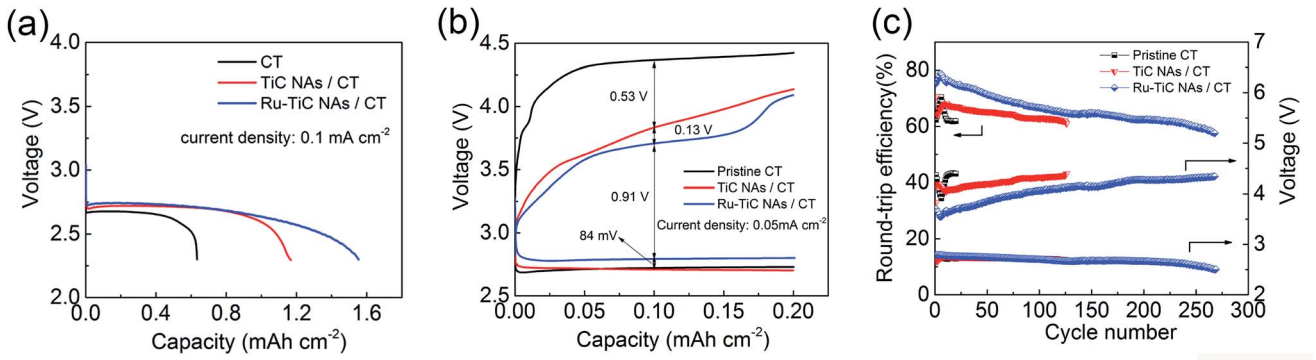

Fig. 6 (a) Full discharge of the Li–O_2 cells with bare CT, as-prepared TiC NAs/CT and Ru–TiC NAs/CT cathodes with a cut-off voltage at 2.3 V and a current density of 0.1 mA cm^{-2}. (b) First discharge–charge curves of the Li–O_2 cells with bare CT, as-prepared TiC NAs/CT and Ru–TiC NAs/CT cathodes at a current density of 0.05 mA cm^{-2}. (c) Round-trip efficiencies and half-capacity voltages for each cycle of the Li–O_2 batteries with pristine CT, TiC NAs/CT and Ru–TiC NAs/CT cathodes at a current density of 0.05 mA cm^{-2} with a limited capacity of 0.2 mA h cm^{-2}.

This journal is © The Royal Society of Chemistry 2018

Open Access Article. Published on 24 October 2018. Downloaded on 6/14/2026 1:53:30 PM.
This article is licensed under a Creative Commons Attribution 3.0 Unported Licence.

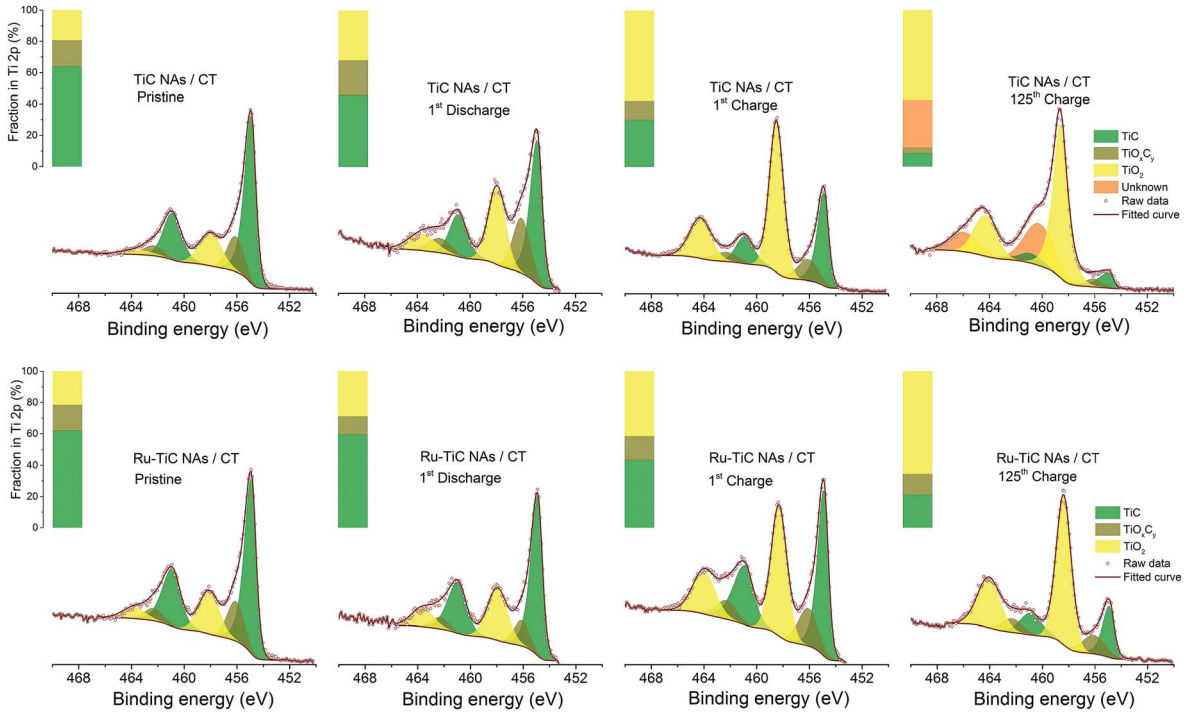

Fig. 7 Ti 2p XPS spectra of TiC NAs/CT and Ru–TiC NAs/CT at different cycle stages.

oxidized layer could be the factor that determines the electron transfer kinetics through it. In this study, due to the surface modification using Ru NPs, we observed better cyclability of the cell with Ru–TiC NAs/CT than that with TiC NAs/CT. To investigate the function of Ru decoration on the TiC surface, XPS measurements were conducted. As shown in Fig. 7, the XPS results indicate that the chemical states of Ti on the two pristine electrodes (TiC NAs/CT and Ru–TiC NAs/CT) were identical (except for the presence of Ru), but their surface chemistry differed after cycling. As calculated from the peak areas of the fitted Ti 2p XPS spectra, the surface ratios of $TiC/TiO_xC_y/TiO_2$ are 0.64 : 0.17 : 0.19 and 0.62 : 0.17 : 0.21 for pristine TiC NAs/CT and pristine Ru–TiC NAs/CT, respectively. However, after the first discharge, the surface ratios of $TiC/TiO_xC_y/TiO_2$ changed to 0.46 : 0.22 : 0.32 and 0.60 : 0.12 : 0.29 for TiC NAs/CT and Ru–TiC NAs/CT, respectively. Without the surface modification using Ru NPs, the proportion of TiO_2 on the TiC NAs/CT cathode increased more quickly and the proportion of TiC decreased faster than on the Ru–TiC NAs/CT cathode during cycling. Combined with the Raman spectrum in Fig. 1h showing a small peak of rutile TiO_2 and the XRD data in Fig. 3a showing only TiC diffraction peaks, we conclude that the surface layer of TiO_2 on the as-prepared TiC is either very thin or amorphous. However, the increased amount of TiO_2 on the surface of TiC NAs/CT during extended cycling hinders electron transfer.[21] After 125 cycles, the TiC NAs/CT cathode surface was dominated by TiO_2 and unknown species, indicated by binding energies around 460 eV and 466 eV, which did not show up in the Ru–TiC NAs/CT sample. We conclude that with Ru modification, the stability of the TiO_2-rich TiC surface was largely improved.

Conclusions

Having a stable cathode material that can promote highly reversible formation and decomposition of Li_2O_2 is one of the key requirements to successfully operate a rechargeable aprotic Li–O_2 cell. As a step towards this goal, we have designed a highly efficient and stable cathode of Ru NP decorated TiC for Li–O_2 batteries, as a free standing electrode. The oriented TiC NAs provide not only a large surface for the deposition of discharge products, but also a pathway for electrical and ionic conduction. In addition, this cathode configuration prevents the direct exposure of carbon to the electrolyte, and ensures reliable electron transfer and structural integrity of the electrode. Furthermore, it avoids unnecessary usage of polymeric binders. The surface of TiC is easily oxidized to form a TiO_2 protective layer during cycling. However, progressive oxidation of the TiC surface should be avoided. Here, we introduce Ru NPs, which not only benefits the discharge and charge process, but also slows down the continuous TiC surface oxidation, increasing the stability of the cathode material. The Ru–TiC NAs/CT cathode demonstrated an improved areal capacity, lower overpotential, longer cyclability, and higher stability towards TiC surface degradation. The high kinetics and efficiency of the formation and decomposition of Li_2O_2 in Ru–TiC NAs/CT based Li–O_2 batteries were confirmed by *in operando* XRD. All of these improvements arise from the integration of favourable compositional and structural properties of the Ru–TiC NAs/CT composite. This study provides a viable approach toward high-performance and stable cathode materials for Li–O_2 batteries.

Open Access Article. Published on 24 October 2018. Downloaded on 6/14/2026 1:53:30 PM.
This article is licensed under a Creative Commons Attribution 3.0 Unported Licence.

Experiments and methods

Synthesis of TiC NAs

The TiC NA preparation was modified from a previously reported work.[50] The synthetic strategy for fabricating TiC NAs/CT cathodes is illustrated in Scheme 1. Briefly, $Ni(NO_3)_2 \cdot 6H_2O$ (30 mg) and NaCl (58 mg) were dissolved in 10 mL of ethanol. 160 mg of TiO_2 powder (anatase, < 25 nm, 99.7%, Aldrich chemistry) was then dispersed into the above solution by ultrasound irradiation for 1 h to form a homogeneous Ni–Ti–Cl emulsion. Then, 300 mg of carbon cloth (pre-punched into a 13 mm diameter disc) was added into the emulsion. After magnetic stirring overnight, the carbon cloth was transferred into an oven, and dried at 60 °C for 2 h to remove ethanol. With nickel, chlorine, and titanium being loaded onto the textile surface, the carbon cloth was placed between two slices of titanium foam, and placed in a graphite crucible covered with a lid. The sample was put into a tube furnace, heated to 1250 °C with a ramp of 5 °C min^{-1}, kept at this temperature for 3 h in pure Ar (100 sccm), and further calcined for 3 h under a continuous flow of 5% H_2/95% Ar gas mixture (5 sccm/95 sccm) to reduce the possible intermediate TiO_x into TiC.

Preparation of the Ru–TiC NAs/CT cathode

The loading of Ru nanoparticles onto the surface of the TiC NAs was carried out *via* a simple impregnation method. The as-prepared TiC NAs were immersed into a 1 mg mL^{-1} $RuCl_3$ (Alfa Aesar) ethanol solution overnight. The obtained electrode was dried in air and calcined at 300 °C for 3 h under a flow of 5% H_2/95% Ar gas mixture at 100 sccm. This work and ref. 50 used different textile templates for TiC synthesis. The main differences between ref. 50 and this work also lie in the deposition of noble metal and the calcination of TiC in a reducing atmosphere.

A cathode loaded with commercial Li_2O_2 was prepared in an argon filled glovebox. Commercial Li_2O_2 powder (90%, Sigma Aldrich) was dispersed in dimethyl carbonate by sonication. The dispersion was added dropwise to the TiC NAs and Ru–TiC NAs/CT cathodes. The loading amount of Li_2O_2 was obtained from the weight gain of each cathode.

Material characterization

SEM and TEM were carried out with a SEM/EDS-Zeiss 1550 microscope operated at 10 kV and a JEOL JEM-2100F microscope operated at 200 kV, respectively. The TEM samples were prepared in an Ar-filled glove box and loaded into a JEOL vacuum transfer holder. TEM images were recorded using a Gatan Ultrascan 1000 or Orius 200D camera. Energy-filtered TEM images were acquired using a Gatan Imaging Filter (GIF Trideim 863). Raman spectra were measured using a Renishaw micro Raman system equipped with a Leica LM optical microscope, a CCD camera and a 532 nm laser source. The chemical composition of the samples was analysed with a Perkin-Elmer 7000 DV ICP-AES, following a total digestion using alkaline fusion ($NaOH–Na_2O_2$). In-house XRD patterns were obtained on a Stoe & Cie GmbH Stadi X-ray powder diffractometer equipped with a Ge monochromator (Cu $K_{\alpha 1}$) operating at 45 kV and 40 mA in transmission mode. A pouch cell was used for this measurement. With a polymer coated thin Al-foil as the pouch material, the pouch cell enabled the X-rays to penetrate (Fig. S10†). The residual ratio of Li_2O_2 was determined in comparison with the constant TiC *via* Rietveld refinement using the FullProf program (calculation details can be found in the ESI†). SR-PXD was performed at beamline I711, MAX II synchrotron with a wavelength (λ) of 0.994 Å at MAX IV Laboratory in Lund, Sweden (Fig. S11†). The *in operando* cell was prepared using a similar design as given in our previous work (Fig. S12†).[38] The cell was mounted in transmission mode with an Oxford diffraction Titan CCD area detector to collect the diffraction patterns. LaB_6 was used to calibrate the diffraction parameters of the instrument. In order to avoid beam damage, measurement with short exposures (30 s) and long waiting times (30 min) was implemented.

Electrochemical measurements

Dimethyl sulfoxide (DMSO, >99.5%, Sigma-Aldrich) was distilled before use and $LiClO_4$ (>99.9%, Sigma-Aldrich) was dried in a vacuum oven inside an Ar-filled glove box. 0.5 M $LiClO_4$/DMSO electrolyte was prepared in an Ar-filled glove box. The water content of the as-prepared electrolyte was less than

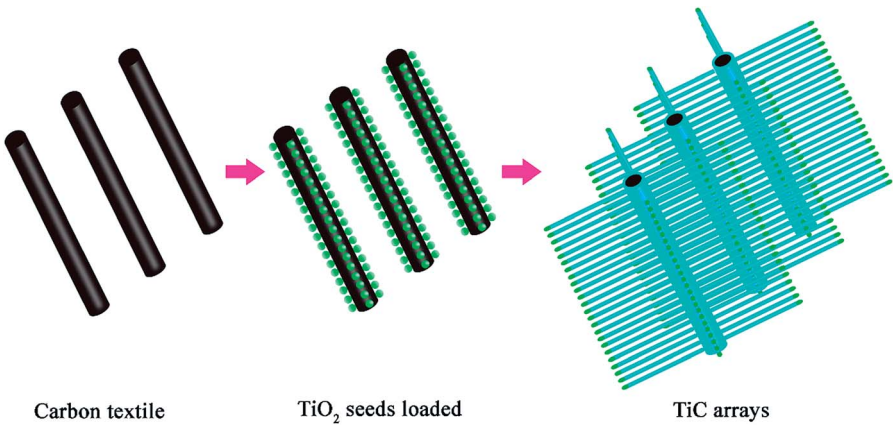

Scheme 1 Schematic illustration of the preparation of TiC NAs.

This journal is © The Royal Society of Chemistry 2018

Open Access Article. Published on 24 October 2018. Downloaded on 6/14/2026 1:53:30 PM. This article is licensed under a Creative Commons Attribution 3.0 Unported Licence.

3 ppm, determined by Karl-Fischer titration. For the electrochemical measurements, Li–O_2 cells were assembled (based on a Swagelok type design) inside an Ar-filled glovebox (O_2 and H_2O < 1 ppm). The cells were composed of a Li metal foil anode (11 mm in diameter and 0.25 mm in thickness), a piece of glass fiber separator (13 mm in diameter), excess electrolyte (0.5 M $LiClO_4$/DMSO), and the as-prepared cathodes. The cells were gas-tightened except for the cathode side being exposed to a pure O_2 atmosphere, and rested for 5 h before testing. Galvanostatic cycling was performed on a Digatron BTS-600 system at a current density of 0.1 mA cm^{-2}. For in-house XRD and SR-PXD measurements, the electrochemical tests were controlled by an external potentiostat (SP-240, Bio-Logic SAS).

Conflicts of interest

There are no conflicts of interest to declare.

Acknowledgements

The authors gratefully appreciate the support for the synchrotron measurement from the MAX-lab staff at beam-line I711. The authors acknowledge the financial support by the Swedish Research Council, Swedish Energy Agency, StandUp for Energy, China Scholarship Council and Opening Project from the Key Laboratory for Ultrafine Materials of the Ministry of Education in the East China University of Science and Technology. Dr Maria Hahlin is gratefully acknowledged for her useful discussion and advice on XPS part. Dr Ismael Saadoune and Dr Rachid Hakkou are greatly acknowledged for their help with the ICP measurement. The authors also thank Dr Jakob Spiegelberg for his help with the *in operando* data refinement.

Notes and references

1 P. G. Bruce, S. A. Freunberger, L. J. Hardwick and J. M. Tarascon, *Nat. Mater.*, 2011, **11**, 19–29.
2 J. M. Tarascon and M. Armand, *Nature*, 2001, **414**, 359–367.
3 B. D. McCloskey, A. Speidel, R. Scheffler, D. C. Miller, V. Viswanathan, J. S. Hummelshoj, J. K. Norskov and A. C. Luntz, *J. Phys. Chem. Lett.*, 2012, **3**, 997–1001.
4 X. Gao, Y. Chen, L. Johnson and P. G. Bruce, *Nat. Mater.*, 2016, **15**, 882–888.
5 B. J. Bergner, A. Schurmann, K. Peppler, A. Garsuch and J. Janek, *J. Am. Chem. Soc.*, 2014, **136**, 15054–15064.
6 F. Li, T. Zhang and H. Zhou, *Energy Environ. Sci.*, 2013, **6**, 1125.
7 H. Geaney and C. O'Dwyer, *J. Electrochem. Soc.*, 2015, **163**, A43–A49.
8 R. Younesi, G. M. Veith, P. Johansson, K. Edström and T. Vegge, *Energy Environ. Sci.*, 2015, **8**, 1905–1922.
9 R. Younesi, M. Hahlin, M. Treskow, J. Scheers, P. Johansson and K. Edström, *J. Phys. Chem. C*, 2012, **116**, 18597–18604.
10 L. J. Hardwick and P. G. Bruce, *Curr. Opin. Solid State Mater. Sci.*, 2012, **16**, 178–185.
11 B. Sun, S. Q. Chen, H. Liu and G. X. Wang, *Adv. Funct. Mater.*, 2015, **25**, 4436–4444.
12 J. Yang, D. Zhai, H. H. Wang, K. C. Lau, J. A. Schlueter, P. Du, D. J. Myers, Y. K. Sun, L. A. Curtiss and K. Amine, *Phys. Chem. Chem. Phys.*, 2013, **15**, 3764–3771.
13 J. Lu, L. Cheng, K. C. Lau, E. Tyo, X. Luo, J. Wen, D. Miller, R. S. Assary, H. H. Wang, P. Redfern, H. Wu, J. B. Park, Y. K. Sun, S. Vajda, K. Amine and L. A. Curtiss, *Nat. Commun.*, 2014, **5**, 4895.
14 M. M. Ottakam Thotiyl, S. A. Freunberger, Z. Peng and P. G. Bruce, *J. Am. Chem. Soc.*, 2013, **135**, 494–500.
15 D. M. Itkis, D. A. Semenenko, E. Y. Kataev, A. I. Belova, V. S. Neudachina, A. P. Sirotina, M. Havecker, D. Teschner, A. Knop-Gericke, P. Dudin, A. Barinov, E. A. Goodilin, Y. Shao-Horn and L. V. Yashina, *Nano Lett.*, 2013, **13**, 4697–4701.
16 Z. Peng, S. A. Freunberger, Y. Chen and P. G. Bruce, *Science*, 2012, **337**, 563–566.
17 J. Xie, X. Yao, I. P. Madden, D. E. Jiang, L. Y. Chou, C. K. Tsung and D. Wang, *J. Am. Chem. Soc.*, 2014, **136**, 8903–8906.
18 M. M. Ottakam Thotiyl, S. A. Freunberger, Z. Peng, Y. Chen, Z. Liu and P. G. Bruce, *Nat. Mater.*, 2013, **12**, 1050–1056.
19 F. Li, D. M. Tang, Y. Chen, D. Golberg, H. Kitaura, T. Zhang, A. Yamada and H. Zhou, *Nano Lett.*, 2013, **13**, 4702–4707.
20 D. Kundu, R. Black, B. Adams, K. Harrison, K. Zavadil and L. F. Nazar, *J. Phys. Chem. Lett.*, 2015, **6**, 2252–2258.
21 B. D. Adams, R. Black, C. Radtke, Z. Williams, B. L. Mehdi, N. D. Browning and L. F. Nazar, *ACS Nano*, 2014, **8**, 12483–12493.
22 A. Y. Kozmenkova, E. Y. Kataev, A. I. Belova, M. Arnati, L. Gregoratti, J. Velasco-Velez, A. Knop-Gericke, B. Senkovsky, D. V. Vyalikh, D. M. Itkis, Y. Shao-Horn and L. V. Yashina, *Chem. Mater.*, 2016, **28**, 8248–8255.
23 C. V. Amanchukwu, J. R. Harding, Y. Shao-Horn and P. T. Hammond, *Chem. Mater.*, 2015, **27**, 550–561.
24 X. J. Feng, K. Zhu, A. J. Frank, C. A. Grimes and T. E. Mallouk, *Angew. Chem., Int. Ed.*, 2012, **51**, 2727–2730.
25 N. K. Shrestha and P. Schmuki, *Electrochemistry*, 2013, **12**, 87–131.
26 X. Xia, J. Tu, Y. Zhang, X. Wang, C. Gu, X. B. Zhao and H. J. Fan, *ACS Nano*, 2012, **6**, 5531–5538.
27 Y.-C. Lu, D. G. Kwabi, K. P. C. Yao, J. R. Harding, J. Zhou, L. Zuin and Y. Shao-Horn, *Energy Environ. Sci.*, 2011, **4**, 2999.
28 M. Leskes, N. E. Drewett, L. J. Hardwick, P. G. Bruce, G. R. Goward and C. P. Grey, *Angew. Chem., Int. Ed. Engl.*, 2012, **51**, 8560–8563.
29 B. M. Gallant, D. G. Kwabi, R. R. Mitchell, J. Zhou, C. V. Thompson and Y. Shao-Horn, *Energy Environ. Sci.*, 2013, **6**, 2518.
30 L. Johnson, C. Li, Z. Liu, Y. Chen, S. A. Freunberger, P. C. Ashok, B. B. Praveen, K. Dholakia, J. M. Tarascon and P. G. Bruce, *Nat. Chem.*, 2014, **6**, 1091–1099.
31 H. Zheng, D. Xiao, X. Li, Y. Liu, Y. Wu, J. Wang, K. Jiang, C. Chen, L. Gu, X. Wei, Y. S. Hu, Q. Chen and H. Li, *Nano Lett.*, 2014, **14**, 4245–4249.
32 S. Ganapathy, B. D. Adams, G. Stenou, M. S. Anastasaki, K. Goubitz, X. F. Miao, L. F. Nazar and M. Wagemaker, *J. Am. Chem. Soc.*, 2014, **136**, 16335–16344.

Open Access Article. Published on 24 October 2018. Downloaded on 6/14/2026 1:53:30 PM.
This article is licensed under a Creative Commons Attribution 3.0 Unported Licence.

33 J. P. Vivek, N. G. Berry, J. Zou, R. J. Nichols and L. J. Hardwick, *J. Phys. Chem. C*, 2017, **121**, 19657–19667.
34 J. L. Shui, J. S. Okasinski, P. Kenesei, H. A. Dobbs, D. Zhao, J. D. Almer and D. J. Liu, *Nat. Commun.*, 2013, **4**, 2255.
35 L. Zhong, R. R. Mitchell, Y. Liu, B. M. Gallant, C. V. Thompson, J. Y. Huang, S. X. Mao and Y. Shao-Horn, *Nano Lett.*, 2013, **13**, 2209–2214.
36 B. D. McCloskey, D. S. Bethune, R. M. Shelby, T. Mori, R. Scheffler, A. Speidel, M. Sherwood and A. C. Luntz, *J. Phys. Chem. Lett.*, 2012, **3**, 3043–3047.
37 H. Lim, E. Yilmaz and H. R. Byon, *J. Phys. Chem. Lett.*, 2012, **3**, 3210–3215.
38 C. Liu, W. R. Brant, R. Younesi, Y. Dong, K. Edström, T. Gustafsson and J. Zhu, *ChemSusChem*, 2017, **10**, 1592–1599.
39 Z. Guo, C. Li, J. Liu, X. Su, Y. Wang and Y. Xia, *J. Mater. Chem. A*, 2015, **3**, 21123–21132.
40 K. R. Yoon, G. Y. Lee, J. W. Jung, N. H. Kim, S. O. Kim and I. D. Kim, *Nano Lett.*, 2016, **16**, 2076–2083.
41 J. R. Harding, Y. C. Lu, Y. Tsukada and Y. Shao-Horn, *Phys. Chem. Chem. Phys.*, 2012, **14**, 10540–10546.
42 M. V. Klein, J. A. Holy and W. S. Williams, *Phys. Rev. B*, 1978, **17**, 1546–1556.
43 X. Y. Tao, J. Du, Y. C. Yang, Y. P. Li, Y. Xia, Y. P. Gan, H. Huang, W. K. Zhang and X. D. Li, *Cryst. Growth Des.*, 2011, **11**, 4422–4426.
44 X. Y. Tao, Y. P. Li, J. Du, Y. Xia, Y. C. Yang, H. Huang, Y. P. Gan, W. K. Zhang and X. D. Li, *J. Mater. Chem.*, 2011, **21**, 9095–9102.
45 R. Younesi, M. Hahlin, F. Björefors, P. Johansson and K. Edström, *Chem. Mater.*, 2013, **25**, 77–84.
46 L. Zhong, R. R. Mitchell, Y. Liu, B. M. Gallant, C. V. Thompson, J. Y. Huang, S. X. Mao and Y. Shao-Horn, *Nano Lett.*, 2013, **13**, 2209–2214.
47 S. Basak, J. Jansen, Y. Kabiri and H. W. Zandbergen, *Ultramicroscopy*, 2018, **188**, 52–58.
48 B. D. Adams, C. Radtke, R. Black, M. L. Trudeau, K. Zaghib and L. F. Nazar, *Energy Environ. Sci.*, 2013, **6**, 1772.
49 R. R. Mitchell, B. M. Gallant, Y. Shao-Horn and C. V. Thompson, *J. Phys. Chem. Lett.*, 2013, **4**, 1060–1064.
50 Z. Qiu, H. Huang, J. Du, X. Tao, Y. Xia, T. Feng, Y. Gan and W. Zhang, *J. Mater. Chem. A*, 2014, **2**, 8003–8008.

This journal is © The Royal Society of Chemistry 2018